Crystal Structure and Melting of Fe Shock Compressed to 273 GPa: *In Situ* X-Ray Diffraction

Stefan J. Turneaure,[1] Surinder M. Sharma,[1] and Y. M. Gupta[1,2]
[1]*Institute for Shock Physics, Washington State University, Pullman, Washington 99164, USA*
[2]*Department of Physics and Astronomy, Washington State University, Pullman, Washington 99164, USA*

(Received 27 July 2020; accepted 23 October 2020; published 18 November 2020)

Despite extensive shock wave and static compression experiments and corresponding theoretical work, consensus on the crystal structure and the melt boundary of Fe at Earth's core conditions is lacking. We present *in situ* x-ray diffraction measurements in laser-shock compressed Fe that establish the stability of the hexagonal-close-packed (hcp) structure along the Hugoniot through shock melting, which occurs between ~242 to ~247 GPa. Using previously reported hcp Fe Hugoniot temperatures, the melt temperature is estimated to be 5560(360) K at 242 GPa, consistent with several reported Fe melt curves. Extrapolation of this value suggests ~6400 K melt temperature at Earth's inner core boundary pressure.

DOI: 10.1103/PhysRevLett.125.215702

Iron is the sixth most abundant element by mass in the Milky Way and among the most common elements in terrestrial planets. The solid inner core and outer molten core of Earth are predominantly composed of Fe, which plays a decisive role in several of Earth's attributes [1–6]. For these reasons, iron has been extensively examined at high *P*-*T* conditions for nearly seven decades. However, the Fe melt curve remains poorly constrained [6] and the Fe crystal structure beyond 200 GPa up to the melt boundary is still not unambiguously determined [7].

Shock wave compression leads to concurrent high *P*-*T* states and has, therefore, played an important role in examining Fe under extreme thermodynamic conditions. Evidence for a high-*P* Fe polymorph was first obtained from shock wave experiments [8], which indicated a large volume change at ~13 GPa along the Hugoniot (locus of *P*-*V* states achieved in shock compression). Subsequently, x-ray diffraction (XRD) measurements under static compression confirmed the high-pressure phase to be the hexagonal-close-packed (hcp) structure [9]. Sound speed measurements in shock compressed Fe to higher stresses have given conflicting results: solid-solid phase transition and melting at 200 and 243 GPa, respectively [10], or only melting over an extended stress range of 225–260 GPa [11]. Analysis of Fe Hugoniot data also suggested a small volume discontinuity near 200 GPa [12]. Optical pyrometry measurements have also been used to determine the temperature of shocked Fe giving widely varying results [13–15]. *In situ* XRD studies in laser-shocked Fe have demonstrated the hcp structure at tens of GPa [16–19] and at two higher stresses (100 and 170 GPa), though with poor signal-to-noise ratio [20]. Two x-ray absorption studies on shocked Fe were interpreted to imply melting at ~260 GPa (XANES) [21] and a close-packed structure [e.g., hcp, face-centered-cubic (fcc) or double-hcp (dhcp)] under multiple shock compression to ~560 GPa (EXAFS) [22]. The EXAFS results have also been interpreted as being consistent with the bcc structure [7].

Static compression studies have comprehensively investigated crystal structures and melting in several regions of the *P*-*T* plane. Figure 1 summarizes the present understanding of the Fe phase diagram, based primarily on static compression studies. Some of the recently reported Fe melt curves under static compression [23,24] and shock compression [15] are in general agreement. However, other reported static compression Fe melt curves are ~700–1000 K lower [25,26] than the results in Refs. [15,23,24], resulting in uncertainty in the Fe melt temperature extrapolated to the inner core boundary (ICB) pressure. In addition to the four well established Fe phases (α, γ, δ, and ε), analysis of static compression measurements has provided evidence for several other possible high *P*-*T* Fe structures: dhcp [27–29], orthorhombic [30], fcc [31], and bcc [32]. Based on theoretical calculations, the bcc structure has been proposed as possibly being entropically stabilized near the Fe melt boundary [7,33,34], but direct experimental evidence is lacking. Experimental results from only two static compression, *in situ* XRD studies have been reported for Fe near the melting temperature beyond 200 GPa and both concluded that Fe has the hcp structure [4,26]. However, the results from Ref. [4] have also been argued to be consistent with the bcc structure [35]. Furthermore, the maximum temperatures reached in both studies [4,26] were well below the melting curve reported in Ref. [23]; the lack of diffuse liquid x-ray scattering data [4,26] raises the question whether the actual melting curve was reached in these static compression experiments. Because of the conflicting inferences and findings summarized above, direct determination of the crystal structure of Fe beyond 200 GPa for temperatures up

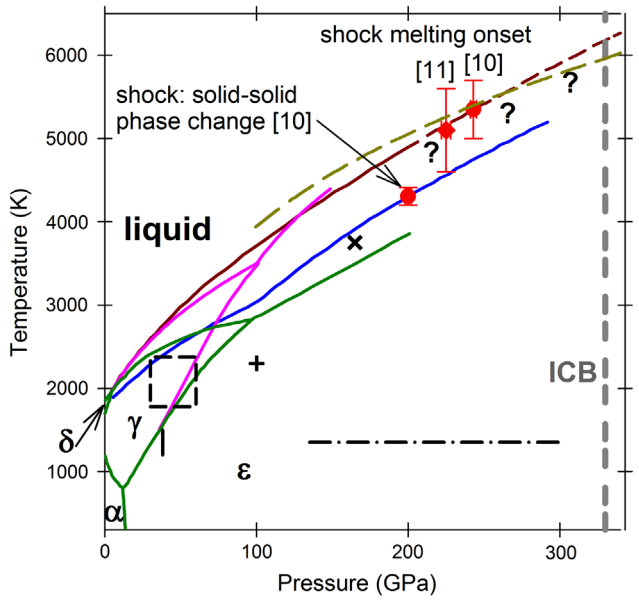

FIG. 1. Phase diagram of iron based on selected past work. Solid colored lines are phase boundaries reported from static compression work: green [25]; dark red [23] with dashed line an extrapolation; pink [24]; blue [26]. The dark yellow dashed line is a reported melt boundary based on a fit to shock compressed Fe pyrometry temperature measurements [15]. Four well established phases are shown: α (bcc); γ (fcc); δ (bcc); ε (hcp). Black lines and symbols represent other reported high P-T Fe structures: dhcp (vertical solid line [27,28]) and horizontal dash-dotted line [29]); orthorhombic (dashed rectangle and crosshair [30]); fcc (cross [31]) which has also been interpreted as bcc [32]. Reported phase transformations inferred from sound speed measurements in shocked Fe are shown by red symbols [10,11]. Vertical dashed line at 330 GPa represents the inner core boundary pressure of Earth.

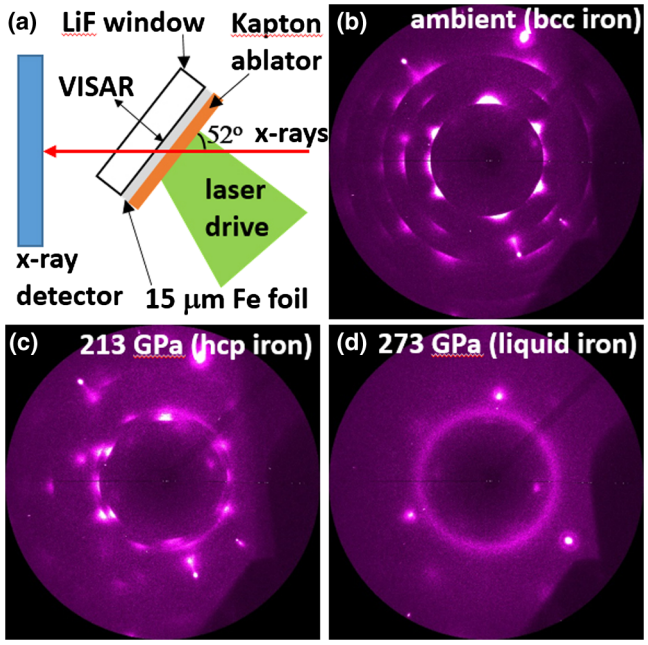

FIG. 2. (a) Experimental configuration for *in situ* XRD and continuum measurements in laser-shocked Fe. (b)–(d) Representative single-pulse XRD patterns. Bright localized spots in the XRD patterns are from the LiF single crystal window.

to the melt boundary remains an important need and is the focus of the present Letter.

Shock compression results in well-defined P-V states along the Hugoniot without the spatial stress and temperature gradients present in static high P-T studies; thus, providing a complementary approach to examine the Fe structure beyond 200 GPa through the melt boundary. We present *in situ* XRD measurements in laser-shock compressed Fe along the Hugoniot through melting. A clear coexistence of hcp Fe diffraction peaks and a diffuse liquid Fe scattering ring are observed from ~242–247 GPa, establishing the stability of the hcp Fe phase through shock melting. Also, our results better constrain the shock melting stress (~225–260 GPa) reported previously [10,11,21] to a narrow stress range ~5 GPa. Knowledge of the Fe structure at the shock melting onset stress (242 GPa) and theoretically calculated hcp Fe Hugoniot temperatures [36–38] provide an anchor point on the hcp-liquid Fe melt boundary.

The experimental configuration used for the present *in situ* XRD measurements to examine phase transformations in laser-shocked Fe is shown in Fig. 2. Eleven experiments were performed at the Dynamic Compression Sector (DCS), located at the Advanced Photon Source, using the DCS 100 J laser as the driver [39]. The targets consisted of a 15-μm thick pure Fe foil sandwiched between a 50-μm thick aluminized Kapton ablator and a ~1-mm thick LiF(100) window. Either a 5-ns duration or a 10-ns duration 500-μm diameter drive laser pulse ablated the Kapton [39] generating a shock wave which propagated through the target. Shock stress was varied by adjusting the drive laser duration and/or using beam splitters to reduce the energy on target. The particle velocity histories at the Fe/LiF interface, recorded using a velocity interferometer [40], are shown in Fig. S1 of the Supplemental Material (SM) [41]. Shock stresses in the Fe were determined from the measured Fe/LiF interface velocities using impedance matching [41].

Single pulse (~100-ps duration) XRD measurements were performed using ~23.56 keV x rays (see Fig. S2 [41]). The x-ray measurements were performed while the shock wave was propagating through the Fe, with at least 86% of the Fe in the shocked state; the fraction of Fe remaining unshocked during the XRD measurement was determined by the intensity of the ambient $(110)_{bcc}$ peak recorded during the shock experiment [41]. Thus, the XRD measurements correspond to diffraction from shocked Fe superposed with a small contribution of diffraction from ambient Fe. More details regarding the experiments are provided in the SM [41].

Figure 2 shows representative XRD patterns recorded for ambient and two shock stresses; Fig. S3 shows XRD

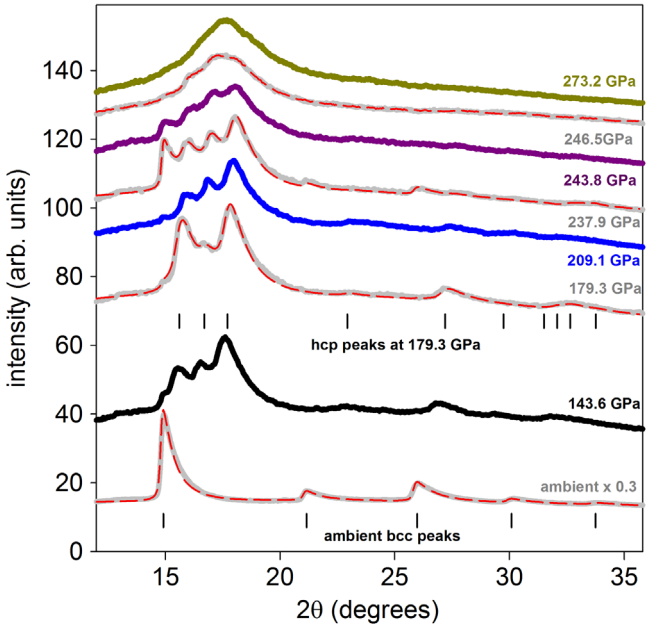

FIG. 3. Representative Fe XRD line profiles. Solid lines are measured and red dashed lines are best fit simulations. Ambient bcc peaks are observed in some of the shocked Fe profiles due to a small thickness of the Fe sample remaining unshocked during the XRD measurement.

patterns for all experiments [41]. The diffraction patterns shown in Fig. 2 represent distinct structural states. At 213 GPa, the Fe diffraction pattern shows a new set of diffraction rings—in contrast to the ambient diffraction pattern—demonstrating a structural transformation. At 273 GPa, sharp diffraction features are absent indicating the molten state of Fe.

The XRD patterns were integrated azimuthally after masking the LiF diffraction spots [41] and representative XRD line profiles at several shock stresses are shown in Fig. 3. To extract structural information for the shock compressed Fe, the measured line profiles are compared with simulated line profiles for various candidate structures. Simulated line profiles incorporate the experimental geometry, the spectral flux shape, and x-ray absorption in the target. More details regarding XRD line profile simulations and comparisons with the measured line profiles are provided in Sec. S4 of the SM [41]. The XRD data were also analyzed to determine anisotropic strains due to material strength in the shocked state. We obtained an upper bound for lattice strain anisotropies of ∼1% (see SM Sec. S5 [41]), in marked contrast to Ref. [22] where large strengths were indirectly concluded for laser-shocked Fe.

The line profiles for Fe shock compressed to 144–242 GPa—prior to the onset of melting—are fully consistent with the hcp structure. The hcp a and c lattice parameters for shocked Fe were determined by fitting hcp Fe line profile simulations to the first three shocked Fe diffraction peaks (see Fig. S5 [41]); higher scattering angle diffraction peaks were not included since they had much lower intensities. Simulated line profiles using the best fit hcp lattice parameters are compared with the measured line profiles for several representative experiments in Fig. 3; excellent agreement with the measured line profiles is observed over the full scattering angle range. The relative textures of the ambient bcc Fe and shocked hcp Fe are also consistent with the orientation relations reported for Fe shocked along [100] at much lower shock stresses [16] (see SM Sec. S6 [41]). Based on the broadening required to match the measured peak widths and the Scherrer equation [48], a lower bound for the coherently diffracting domain size (CDDS) of the hcp Fe is ∼6–7 mm for experiments from 144–242 GPa. These values are similar to the CDDS (2–15 nm) reported for hcp Fe in laser-shock experiments with peak stress below 20 GPa [17].

Our measured XRD line profiles for laser-shocked Fe are very different from those expected for fcc or bcc phases (see Figs. S9 and S10) ruling out these crystal structures. Furthermore, for the dhcp and orthorhombic structures several predicted peaks are not observed or are at the wrong scattering angle, also ruling out these two structures. These findings, along with the excellent match between simulated hcp Fe line profiles and measured line profiles, prove that shocked Fe remains hcp to 242 GPa and rules out the purported solid-solid phase transformation at 200 GPa [10].

Between 242–247 GPa, significant changes in the XRD patterns occur when compared to the patterns at lower stresses. We note that fitting the measured line profiles to a pure hcp structure results in good fits, but with a large increase in the amount of line broadening compared to experiments at lower stresses (see Figs. S5 and S6). Visual inspection of the XRD patterns in Fig. S11 shows the emergence of a smooth broad diffraction ring above 242 GPa. We also note that the shock stress variation with increasing laser energy shows a plateau over this stress region (see Fig. S12); such a plateau is expected while the Hugoniot follows the melt boundary due to the latent heat of melting. Based on these observations, we conclude that the observed increase in the width of the hcp diffraction peaks (see Fig. S6) for the 242.4–246.5 GPa experiments is due to a broad liquid scattering ring superposed on the first three hcp peaks—due to partial melting of the shocked Fe. To determine the hcp lattice parameters in this mixed phase region, the measured line profiles were fit to a superposition of simulated crystalline Fe diffraction peaks (including the first three hcp peaks) and a line profile corresponding to liquid Fe scattering (see SM Sec. S4 [41]). The resulting fits are shown in Fig. S5. Using the best fit hcp Fe lattice parameters in the simulations superposed with the liquid Fe scattering line profile resulted in excellent agreement between measured and simulated line profiles in the mixed phase region over the entire scattering angle range; a representative example (246.5 GPa peak stress) is shown in Fig. 3.

The Fe specific volume V was calculated from the best fit hcp a and c lattice parameters. Shock stress vs V/V_0 is plotted in Fig. 4(a); V_0 is the ambient specific volume of bcc Fe. The XRD volumes determined from our work are in excellent agreement with previous densities for shocked Fe determined using continuum shock wave measurements [42]. However, we note that the hcp XRD volumes in the mixed phase region are at slightly lower values than those obtained from the continuum Hugoniot [42]; this observation is consistent with the liquid Fe having a larger volume than the hcp Fe as required due to the positive melting Clapeyron slope for Fe. The hcp iron c/a ratios determined from our XRD analysis are nearly independent of the shock stress, with values ranging from 1.619–1.627 (see Table S1).

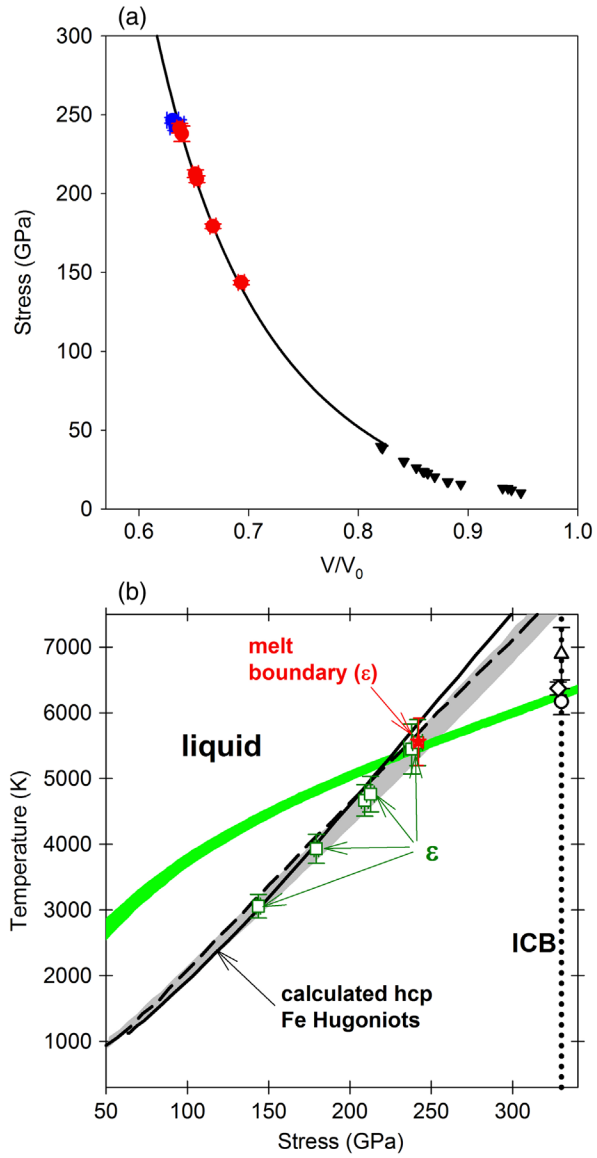

FIG. 4. (a) Stress-volume for shock-compressed Fe. Red symbols (present work) are XRD densities for Fe shock compressed to the hcp phase. Blue symbols are hcp Fe densities (present work) for Fe shock compressed into an hcp-liquid mixed phase (above 242 GPa). Line is from analysis of continuum Fe Hugoniot data [42]. Black triangles are lower stress continuum results [49]. (b) Iron phase diagram. Green squares are present results for hcp (ε) iron up to the onset of shock melting at ~242 GPa (red star); temperatures are the average of the minimum and maximum calculated hcp Fe Hugoniot temperatures (two black lines and gray band) in Refs. [36–38] with uncertainties encompassing the maximum and minimum calculated temperatures. The green band is from the theoretical Fe melt curve [50] that passes closest to our melt boundary data point and the black symbols are theoretical Fe melt temperatures near the inner-core boundary (ICB) pressure: circle [51]; diamond [52]; triangle [53].

Our *in situ* XRD measurements indicate a narrow stress range for shock melting: 242(3)–247(3) GPa. Estimates of the volume fractions of liquid iron vs shock stress using several approaches are shown in Fig. S13 [41]. The narrow stress range observed for shock melting in our work greatly constrains the shock melting stress of Fe relative to past experimental work [10,11,21]. Having established that shock-induced melting of Fe occurs from the hcp phase with an onset stress of ~242(3) GPa, we used theoretical calculations for the P-T states along the Hugoniot of hcp Fe to determine the temperature corresponding to shock melting onset. This approach is expected to be more accurate than the calculated theoretical melt boundary curves based on Gibbs free energies because of the following reason. The temperature dependent energies of hcp Fe and liquid Fe cross with shallow slopes at a fixed pressure making the calculated melting temperatures quite sensitive to small errors in the calculated energies [50,51]; calculated theoretical melt curves for Fe differ by ~1000 K [50,54]. In contrast, three independent theoretical hcp Fe Hugoniot calculations predict similar temperatures as shown in Fig. 4(b); these results are also consistent with other Hugioniot temperature calculations and recent Fe Hugoniot temperature measurements as shown in Fig. S15 [41]. For shock stresses between 239–245 GPa, the calculated hcp Fe Hugoniot temperature is 5560(360) K [36–38] and our resulting Fe melt boundary point (242 GPa, 5560 K) is denoted by the red star in Fig. 4(b).

We compare our melt boundary point with existing theoretical [50,54] and experimental Fe melt curves [23–26] and pyrometry temperature results in shocked Fe [13–15] (see Fig. S16 [41]). Our result strongly supports the melt curves reported by Anzellini *et al.* [23] and Alfe *et al.* [50] and shows significant disagreement with the lower temperature melt curves from Refs. [25,26,54]. Our result is also consistent with recent pyrometry temperature measurements [15] but is significantly lower than early pyrometry measurements [13,14].

All existing estimates of the Fe melting temperature at the ICB pressure, from experiments, are based on extrapolations. We note that the theoretical Fe melt curve [50] passing through our melt boundary point has a very similar slope to the experimental melt curve reported by Anzellini

et al. [23] above 150 GPa (see Fig. S16). Thus, the theoretical melt curve from Ref. [50] shown in Fig. 4(b) provides a useful approach to extrapolate the Fe melt temperature from 242 to 330 GPa. This results in a ~6400 K melt temperature for pure Fe at 330 GPa, the pressure at the Earth's inner core boundary. This temperature is close to several *ab initio* iron melting temperature calculations [51–53] near 330 GPa [see Fig. 4(b)].

Using synchrotron-based XRD measurements in well-characterized shock compression experiments, the crystal structure and the melting transition of Fe were examined at extreme *P-T* conditions. High quality XRD data were obtained in the solid phase, solid-liquid phase, and upon complete melting. The present work has established the stability of the hcp phase up to the onset of melting at 242 GPa. The mixed phase region, with clear hcp-liquid Fe coexistence, was observed over a narrow stress range ~5 GPa. These two findings are in marked contrast to conclusions from earlier shock experiments—that utilized sound speed measurements—regarding a solid-solid transition at 200 GPa [10] and the occurrence of melting over a broad stress range ~35 GPa [11]. Thus, the interpretation of sound speed measurements to infer material response regarding shock-induced phase transition, including melting, may require further examination. Our results also suggest that the Fe melt temperature at the inner core boundary pressure is significantly higher than the values inferred from several static pressure studies [25,26], but is in good agreement with other static compression results [23] and several theoretical Fe melt temperatures [51–53].

Pinaki Das, Yuelin Li, Drew Rickerson, Paulo Rigg, Adam Schuman, Nick Sinclair, Xiaoming Wang, and Jun Zhang at the Dynamic Compression Sector (Advanced Photon Source, Argonne National Laboratory) are gratefully acknowledged for their assistance with the experiments. Yoshi Toyoda is thanked for assistance with analysis of velocity interferometry data. This Letter is based upon work supported by the U.S. Department of Energy (DOE), National Nuclear Security Administration (NNSA) under Awards No. DE-NA0002007 and No. DE-NA0003957. This publication is also based upon work performed at the Dynamic Compression Sector, operated by Washington State University under DOE/NNSA Award No. DE-NA0002442. This research used resources of the Advanced Photon Source, a DOE Office of Science User Facility operated for the DOE Office of Science by Argonne National Laboratory under Contract No. DE-AC02-06CH11357.

[1] B. A. Buffett, Science **288**, 2007 (2000).
[2] K. C. Creager, Nature (London) **356**, 309 (1992).
[3] A. B. Belonoshko, N. V. Skorodumova, A. Rosengren, and B. Johansson, Science **319**, 797 (2008).
[4] S. Tateno, K. Hirose, Y. Ohishi, and Y. Tatsumi, Science **330**, 359 (2010).
[5] R. J. Hemley and H.-K. Mao, Int. Geol. Rev. **43**, 1 (2001).
[6] R. A. Fischer, in *Deep Earth: Physics and Chemistry of the Lower Mantle and Core*, edited by H. Terasaki and R. A. Fischer (John Wiley and Sons, Hoboken, NJ, 2016), pp. 3–12.
[7] A. B. Belonoshko, T. Lukinov, J. Fu, J. Zhao, S. Davis, and S. I. Simak, Nat. Geosci. **10**, 312 (2017).
[8] D. Bancroft, E. L. Peterson, and S. Minshall, J. Appl. Phys. **27**, 291 (1956).
[9] R. L. Clendenen and H. G. Drickamer, J. Phys. Chem. Solids **25**, 865 (1964).
[10] J. M. Brown and R. G. McQueen, J. Geophys. Res. **91**, 7485 (1986).
[11] J. H. Nguyen and N. C. Holmes, Nature (London) **427**, 339 (2004).
[12] J. M. Brown, Geophys. Res. Lett. **28**, 4339 (2001).
[13] J. D. Bass, B. Svendsen, and T. J. Ahrens, in *High Pressure Research in Mineral Physics*, edited by M. H. Manghanani and Y. Syono (American Geophysical Union, Washington, DC, 1987), pp. 393–402.
[14] C. S. Yoo, N. C. Holmes, M. Ross, D. J. Webb, and C. Pike. Phys. Rev. Lett. **70**, 3931 (1993).
[15] J. Li, Q. Wu, J. Li, T. Xue, Y. Tan, X. Zhou, Y. Zhang, Z. Xiong, Z. Gao, and T. Sekine, Geophys. Res. Lett. **47**, e2020GL087758 (2020).
[16] D. H. Kalantar, J. F. Belak, G. W. Collins, J. D. Colvin, H. M. Davies, J. H. Eggert, T. C. Germann, J. Hawreliak, B. L. Holian, K. Kadau, P. S. Lomdahl, H. E. Lorenzana, M. A. Meyers, K. Rosolankova, M. S. Schneider, J. Sheppard, J. S. Stölken, and J. S. Wark, Phys. Rev. Lett. **95**, 075502 (2005).
[17] J. A. Hawreliak, D. H. Kalantar, J. S. Stölken, B. A. Remington, H. E. Lorenzana, and J. S. Wark, Phys. Rev. B **78**, 220101(R) (2008).
[18] J. A. Hawreliak, B. El-Dasher, H. Lorenzana, G. Kimminau, A. Higginbotham, B. Nagler, S. M. Vinko, W. J. Murphy, T. Whitcher, J. S. Wark, S. Rothman, and N. Park, Phys. Rev. B **83**, 144114 (2011).
[19] H. Hwang *et al.*, Sci. Adv. **6**, eaaz5132 (2020).
[20] A. Denoeud, N. Ozaki, A. Benuzzi-Mounaix, H. Uranishi, Y. Kondo, R. Kodama, E. Brambrink, A. Ravasio, M. Bocoum, J.-M. Boudenne, M. Harmand, F. Guyot, S. Mazevet, D. Riley, M. Makita, T. Sano, Y. Sakawa, Y. Inubushi, G. Gregori, M. Koenig, and G. Morard, Proc. Natl. Acad. Sci. U.S.A. **113**, 7745 (2016).
[21] M. Harmand, A. Ravasio, S. Mazevet, J. Bouchet, A. Denoeud, F. Dorchies, Y. Feng, C. Fourment, E. Galtier, J. Gaudin, F. Guyot, R. Kodama, M. Koenig, H. J. Lee, K. Miyanishi, G. Morard, R. Musella, B. Nagler, M. Nakatsutsumi, N. Ozaki, V. Recoules, S. Toleikis, T. Vinci, U. Zastrau, D. Zhu, and A. Benuzzi-Mounaix, Phys. Rev. B **92**, 024108 (2015).
[22] Y. Ping, F. Coppari, D. G. Hicks, B. Yaakobi, D. E. Fratanduono, S. Hamel, J. H. Eggert, J. R. Rygg, R. F. Smith, D. C. Swift, D. G. Braun, T. R. Boehly, and G. W. Collins, Phys. Rev. Lett. **111**, 065501 (2013).
[23] S. Anzellini, A. Dewaele, M. Mezouar, P. Loubeyre, and G. Morard, Science **340**, 464 (2013).

[24] G. Morard, S. Boccato, A. D. Rosa, S. Anzellini, F. Miozzi, L. Henry, G. Garbarino, M. Mezouar, M. Harmond, F. Guyot, E. Boulard, I. Kantor, T. Irifune, and R. Torchio, Geophys. Res. Lett. **45**, 11074 (2018).
[25] R. Boehler, Nature (London) **363**, 534 (1993).
[26] R. Sinmyo, K. Hirose, and Y. Ohishi, Earth Planet. Sci. Lett. **510**, 45 (2019).
[27] S. K. Saxena, L. S. Dubrovinsky, P. Häggkvist, Y. Cerenius, G. Shen, and H. K. Mao, Science **269**, 1703 (1995).
[28] C. S. Yoo, J. Akella, A. J. Campbell, H. K. Mao, and R. J. Hemley, Science **270**, 1473 (1995).
[29] L. S. Dubrovinsky, S. K. Saxena, F. Tutti, S. Rekhi, and T. LeBehan, Phys. Rev. Lett. **84**, 1720 (2000).
[30] D. Andrault, G. Fiquet, M. Kunz, F. Visocekas, and D. Häusermann, Science **278**, 831 (1997).
[31] A. S. Mikhaylushkin, S. I. Simak, L. Dubrovinsky, N. Dubrovinskaia, B. Johansson, and I. A. Abrikosov, Phys. Rev. Lett. **99**, 165505 (2007).
[32] A. B. Belonoshko, P. M. Derlet, A. S. Mikhaylushkin, S. I. Simak, O. Hellman, L. Burakovsky, D. C. Swift, and B. Johansson, New J. Phys. **11**, 093039 (2009).
[33] M. Ross, D. A. Young, and R. Grover, J. Geophys. Res. **95**, 21713 (1990).
[34] A. B. Belonoshko, R. Ahuja, and B. Johansson, Nature (London) **424**, 1032 (2003).
[35] L. Dubrovinsky, N. Dubrovinskaia, and V. Prakapenka, Fisica de la Tierra **23**, 73 (2011).
[36] E. Wasserman, L. Stixrude, and R. E. Cohen, Phys. Rev. B **53**, 8296 (1996).
[37] D. Alfe, G. D. Price, and M. J. Gillan, Phys. Rev. B **64**, 045123 (2001).
[38] X. Sha and R. E. Cohen, Phys. Rev. B **81**, 094105 (2010).
[39] X. Wang, P. Rigg, J. Sethian, N. Sinclair, N. Weir, B. Williams, J. Zhang, J. Hawreliak, Y. Toyoda, Y. Gupta, Y. Li, D. Broege, J. Bromage, R. Earley, D. Guy, and J. Zuegel, Rev. Sci. Instrum. **90**, 053901 (2019).
[40] L. M. Barker and R. E. Hollenbach, J. Appl. Phys. **43**, 4669 (1972).
[41] See Supplemental Material at http://link.aps.org/supplemental/10.1103/PhysRevLett.125.215702 for additional experimental details, velocity interferometry results, analysis of velocity interferometry data to obtain shock stresses, additional XRD results, and analysis details, which includes Refs. [42–47].
[42] J. M. Brown, J. N. Fritz, and R. S. Hixson, J. Appl. Phys. **88**, 5496 (2000).
[43] Q. Liu, X. Zhou, X. Zeng, and S. N. Luo, J. Appl. Phys. **117**, 045901 (2015).
[44] A. P. Hammersley, FIT2D: An introduction and overview, ESRF Internal Report No. ESRF97HA02T, 1997.
[45] A. P. Hammersley, S. O. Svensson, M. Hanfland, A. N. Fitch, and D. Hausermann, High Press. Res. **14**, 235 (1996).
[46] D. A. Boness and J. M. Brown, J. Geophys. Res. **95**, 21721 (1990).
[47] R. Torchio *et al.*, Sci. Rep. **6**, 26402 (2016).
[48] B. E. Warren, *X-Ray Diffraction* (Addison-Wesley, Reading, 1969).
[49] L. M. Barker and R. E. Hollenbach, J. Appl. Phys. **45**, 4872 (1974).
[50] D. Alfe, G. D. Price, and M. J. Gillan, Phys. Rev. B **65**, 165118 (2002).
[51] T. Sun, J. P. Brodholt, Y. Li, and L. Vocadlo, Phys. Rev. B **98**, 224301 (2018).
[52] D. Alfe, Phys. Rev. B **79**, 060101(R) (2009).
[53] E. Sola and D. Alfe, Phys. Rev. Lett. **103**, 078501 (2009).
[54] A. Laio, S. Bernard, G. L. Chiarotti, S. Scandolo, and E. Tosatti, Science **287**, 1027 (2000).